Eur. J. Mineral., 38, 249–262, 2026
https://doi.org/10.5194/ejm-38-249-2026
© Author(s) 2026. This work is distributed under
the Creative Commons Attribution 4.0 License.

European Journal of Mineralogy
Open Access

The Tibet leucogranite as a potential high-purity-quartz raw material: first discovery and case study from the Dinggye area

Liting Sun[1], Xiaoyong Yang[1,2,3], Mei Xia[1], Yue Qiu[1], Zhenhui Hou[1], Xiaohu Fu[4], and Zetai Chen[4]

[1]State Key Laboratory of Lithospheric and Environmental Coevolution, University of Science and Technology of China, Hefei 230026, China
[2]Hebei Key Laboratory of Strategic Critical Mineral Resources, Hebei GEO University, Shijiazhuang 050031, China
[3]College of Earth Sciences, Hebei GEO University, Shijiazhuang 050031, China
[4]Research Center of Applied Geology of China Geological Survey, Chengdu 610299, China

Correspondence: Xiaoyong Yang (xyyang@ustc.edu.cn) and Mei Xia (xm851102@ustc.edu.cn)

Received: 11 September 2025 – Revised: 29 March 2026 – Accepted: 8 April 2026 – Published: 30 April 2026

Abstract. This study evaluates Tibet leucogranites as a potential raw material for high-purity quartz. We systematically investigate the petrography, geochemistry, and purification potential of leucogranites from the Ama Drime Massif of the Dinggye area. Our results demonstrate that these leucogranites hold considerable potential to produce high-purity quartz with SiO_2 contents above 99.995 %, highlighting their value as a new and extensive source of high-purity quartz in Tibet. Various analytical techniques, including optical microscopy, X-ray fluorescence imaging, X-ray fluorescence spectrometry, ICP-MS, and LA-ICP-MS, together with purification experiments, were applied to representative samples (XZ-BG and XZ-WJ). The results indicate that the leucogranites are composed predominantly of quartz, albite, and K-feldspar, with minor biotite, muscovite, garnet, and amphibole. These rocks display typical S-type granite characteristics and were likely derived from source regions comprising granitic gneiss and metamorphic shale. Quartz-hosted inclusions are dominated by relatively large primary inclusions and secondary fluid inclusions, which are comparatively easy to remove during purification. As a result, the purified samples yielded SiO_2 contents of 99.996 % and 99.995 %, respectively. This work represents the first integrated mineralogical, geochemical, and purification assessment of Tibet leucogranites as a source of high-purity quartz and proposes temperature as a key ore-controlling factor. The widespread exposure of leucogranite in the region offers a significant opportunity to develop high-end quartz resources in China, ensuring a stable and strategic supply of high-purity-quartz raw materials.

1 Introduction

High-purity quartz (HPQ), defined as having total chemical impurities of less than 50 $\mu g\,g^{-1}$, is a critical mineral supporting strategic emerging industries (Müller et al., 2012). However, global HPQ resources are scarce and highly unevenly distributed, leading to significant supply chain risks (Zhou et al., 2023; Harben, 1995; Hao et al., 2020). The search for new HPQ resources is urgent, and the core scientific challenge lies in identifying geological bodies and metallogenic mechanisms capable of forming ultra-high-purity quartz. Leucogranite, a typical S-type crustal anatectic product in the Himalayan orogenic belt (Magar et al., 2024), is regarded to be a potential source rock for HPQ due to its inherently low impurity content. The widely distributed leucogranites in the Tibet region of China (Cao et al., 2022) provide an ideal research target for achieving breakthroughs in HPQ resources and ensuring national resource security. However, current research has primarily focused on their metal mineralization potential, while systematic evaluation of their HPQ potential remains lacking. To address this, this study focuses on evaluating the HPQ potential of Ti-

betan leucogranites. By integrating geology, geochemistry, and micro-scale lattice analysis, we aim to establish a comprehensive evaluation framework from macro- to micro-scale perspectives. This research not only seeks to fill the gap in HPQ studies in this region but also aims to provide scientific support for enhancing China's autonomous supply capacity of HPQ resources.

2 Geological background and sample collection

The Himalayan orogenic belt was formed by the northward convergence of the Indian Plate and its subsequent collision with the Eurasian Plate along the Yarlung Zangbo suture zone (Yin, 2006; Najman et al., 2010), representing one of the most significant tectonic events since the Cenozoic Era. From north to south, the Himalayan orogenic belt can be subdivided into the Tethys Himalaya, Greater Himalaya, and Lesser Himalaya on the basis of the South Tibet Detachment System (STDS), the Main Central Thrust (MCT), and the Main Boundary Thrust (MBT) (DiPietro and Pogue, 2004) (Fig. 1a). The Himalayan orogenic belt contains extensive Cenozoic leucogranites, forming two world-class belts: the Tethys Himalaya leucogranite belt (northern belt) and the Greater Himalaya leucogranite belt (southern belt) (Zhang et al., 2012; Zhou et al., 2021). Both belts exhibit broadly similar mineral compositions, typically comprising quartz, K-feldspar, plagioclase, biotite, muscovite, tourmaline, and garnet, resulting in highly comparable lithological characteristics. In China, the principal leucogranite intrusions are distributed in the Greater Himalaya mainly exposed in the Gyirong, Nyalam, Dinggye, Yadong, Khula Kangri, and Luozha regions (Wu et al., 2015).

The Dinggye area lies within the central segment of the Greater Himalaya leucogranite belt (Fig. 1b) and represents a dome structure with a north–south-trending long axis characterized by multilayer extensional tectonic assemblages (Yu et al., 2011). The dome is bounded by the Dinggye normal fault to the west and the Ama Drime Massif (ADM) normal fault to the east. Previous studies indicate that the ADM can be subdivided into two lithotectonic units: (1) the northern paragneiss unit, dominated by biotite gneiss and mica schist, and (2) the southern orthogneiss unit, consisting mainly of granite gneiss and migmatite with minor biotite gneiss (Wang et al., 2017a; Langille et al., 2010). In the northern part of the ADM, the paragneiss unit is locally intruded by leucogranitic bodies, indicating that it acted as a wall-rock host for leucogranite emplacement (Gu et al., 2022). Published SHRIMP zircon U–Pb ages from leucogranites in the Dinggye area indicate two Early Miocene magmatic episodes at 21.0±0.7 and 15.8±0.1 Ma, suggesting at least two pulses of leucogranite emplacement (Yu et al., 2011).

The samples in this study were collected from the northern Dinggye area (Fig. 1a). Regionally, the leucogranites in this belt can be divided into two main facies: the Li–F-rich rare-metal-bearing facies and the volatile-poor two-mica leucogranite facies (Wang et al., 2017b). The former is highly differentiated and characterized by magmatic–hydrothermal mineralization, while the latter is poor in rare metals and occurs as large-scale, lithologically homogeneous outcrops (Hou et al., 2011). Samples XZ-BG and XZ-WJ both belong to the muscovite leucogranite of volatile-poor two-mica leucogranite facies and were collected from the same representative outcrop. Despite their spatial proximity, they reflect internal mineralogical heterogeneity, with XZ-BG representing a garnet-rich variety and XZ-WJ representing a garnet-poor variety. The volatile-poor facies studied here is more favorable for high-purity-quartz formation because its relatively clean magmatic system and stable crystallization process are less conducive to lattice impurity enrichment.

3 Analytical methods

First, thin sections were prepared from representative leucogranite samples and examined using transmitted polarized light microscopy (TPM) and X-ray fluorescence (XRF) spectroscopic imaging for detailed petrographic characterization, including mineral assemblages, fracture networks, modal abundances, and spatial distributions. Selected leucogranite samples were then analyzed for whole-rock major element compositions by XRF. In situ trace element analyses of quartz grains were conducted using LA-ICP-MS. Quartz grains isolated during the purification process were mounted on glass slides, treated with a drop of kerosene, and examined under an optical microscope to observe inclusions. The remaining leucogranite samples underwent high-purity-quartz (HPQ) purification via a sequence of crushing, sieving, magnetic separation, hot-acid leaching, and chlorination, with detailed procedures provided in the Supplement. The bulk chemical compositions of the purified quartz sands were determined by ICP-MS, and quartz crystallization temperatures were estimated using the Ti-in-quartz geothermometer. Complete analytical conditions, instrumental parameters, and calculation methods are described in the Supplement.

4 Results

4.1 Petrography of the samples

The petrological characteristics of the leucogranite samples were investigated using both transmitted light microscopy (Fig. 2) and X-ray fluorescence (XRF) spectroscopic imaging (Fig. 3). It should be noted that the XRF spectroscopic imaging and microscopic observations were performed on sections of different thicknesses from the same samples. Consequently, certain low-abundance minerals that could not be fully resolved or mapped in the XRF imagery were clearly observable under the microscope, resulting in slight discrepancies in the accessory mineral assemblages between the two methods.

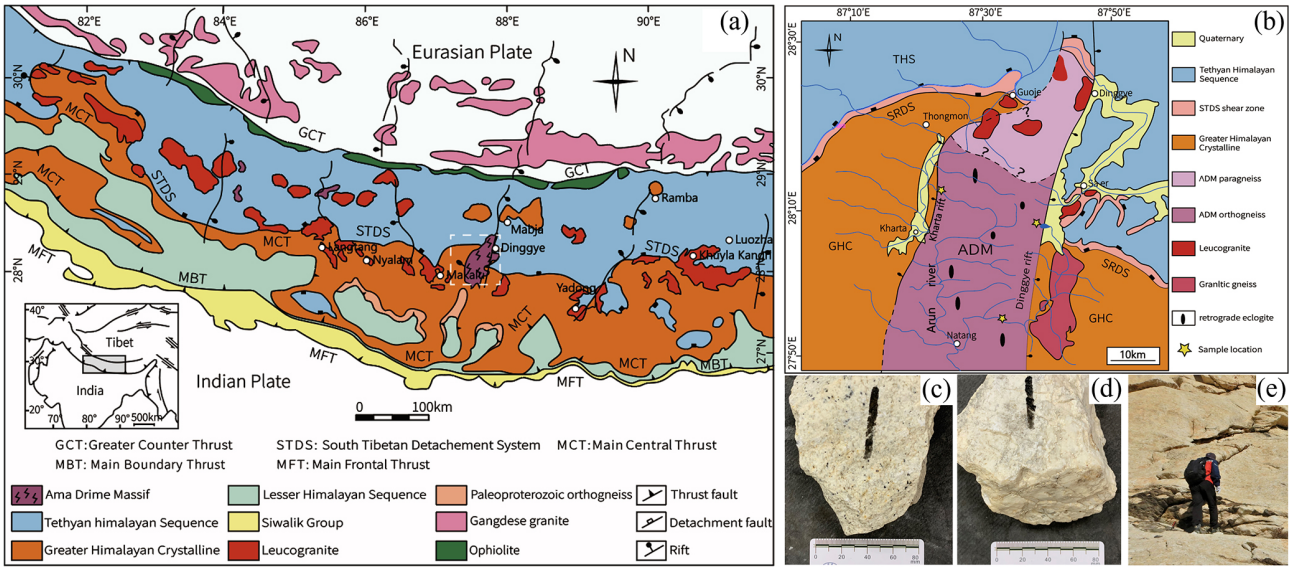

Figure 1. **(a)** Geological map of the Himalayan orogenic belt in southern Tibet (Gu et al., 2022). **(b)** Detailed geological map of the Dinggye area (Gu et al., 2022). **(c)** Hand specimen photo of XZ-BG. **(d)** Hand specimen photo of XZ-WJ. **(e)** Field characteristics of leucogranite outcrop.

Results show that sample XZ-BG is mainly composed of albite (35.61 wt %), quartz (31.75 wt %), and K-feldspar (26.86 wt %), with minor garnet (3.29 wt %), muscovite (3.28 wt %), and apatite (0.02 wt %). Under transmitted light, K-feldspar commonly exhibits a turbid appearance, and quartz inclusions can occasionally be observed within the grains (Fig. 2a). Twinning is commonly developed in albite (Fig. 2b). Quartz mainly occurs as anhedral granular crystals, characterized by abundant internal fractures, undulose extinction, and local dissolution textures. Muscovite typically occurs as flakes distributed along grain boundaries or filling fractures and displays golden-yellow, rose-red, or blue-violet interference colors under crossed polars. In addition, a small amount of amphibole is present (Fig. 2c) as anhedral grains showing golden-yellow pleochroism under plane-polarized light.

Sample XZ-WJ is dominated by quartz (33.64 wt %) and albite (32.18 wt %), followed by K-feldspar (17.99 wt %) and muscovite (13.42 wt %), with minor chlorite (2.69 wt %) and apatite (0.08 wt %). Quartz grains are generally coarser and better preserved, mostly ranging from 50 to 600 µm, with some grains reaching up to 7 mm, and locally showing dissolution by feldspars. Albite and K-feldspar are mostly subhedral and generally coarser than quartz (100–1000 µm) and may locally enclose quartz. Muscovite is relatively abundant and commonly occurs as elongate flakes. Garnet is scarce in this sample (0.08 wt %), and fractures are commonly filled with biotite (Fig. 2e).

Overall, the two samples show distinct petrographic differences. Compared with XZ-WJ, quartz in XZ-BG is generally finer-grained and more strongly affected by internal fracturing and undulose extinction, whereas XZ-WJ is characterized by coarser and better-preserved quartz, together with a markedly higher abundance of muscovite.

4.2 Whole-rock major element abundances

The major element compositions of the two samples are summarized in Table 1. XZ-BG contains 74.68 % SiO_2 and is enriched in total alkalis (ALK = 8.65 %), with $K_2O/Na_2O = 1.57$ and $Al_2O_3 = 14.78$ %. MgO is very low (0.099 %), whereas CaO and Fe_2O_3 are 0.25 % and 0.55 %, respectively. XZ-WJ contains 73.73 % SiO_2 and also has high total alkalis (ALK = 8.85 %) but with Na_2O exceeding K_2O ($K_2O/Na_2O = 0.72$) and slightly higher Al_2O_3 (15.16 %). Its MgO, Fe_2O_3, and CaO contents are 0.055 %, 0.11 %, and 0.28 %, respectively. Both samples have high A / CNK values (1.262 and 1.167), indicating peraluminous compositions, and plot in the high-K calc-alkaline S-type granite field (Fig. S2 in the Supplement).

4.3 Trace element compositions of quartz determined by LA-ICP-MS

In situ LA-ICP-MS spot analyses were performed on quartz grains from samples XZ-WJ and XZ-BG. The analytical results are reported in Table 2, and element–element plots based on individual spot data are provided in the Supplement (Fig. S3).

Quartz samples from XZ-BG contain 4.56–12.70 ppm Li, 3.06–36.91 ppm Na, and 40.92–72.59 ppm Al, with average concentrations of 7.82, 15.30, and 62.69 ppm, respectively. Ti concentrations range from 4.64 to 9.16 ppm, av-

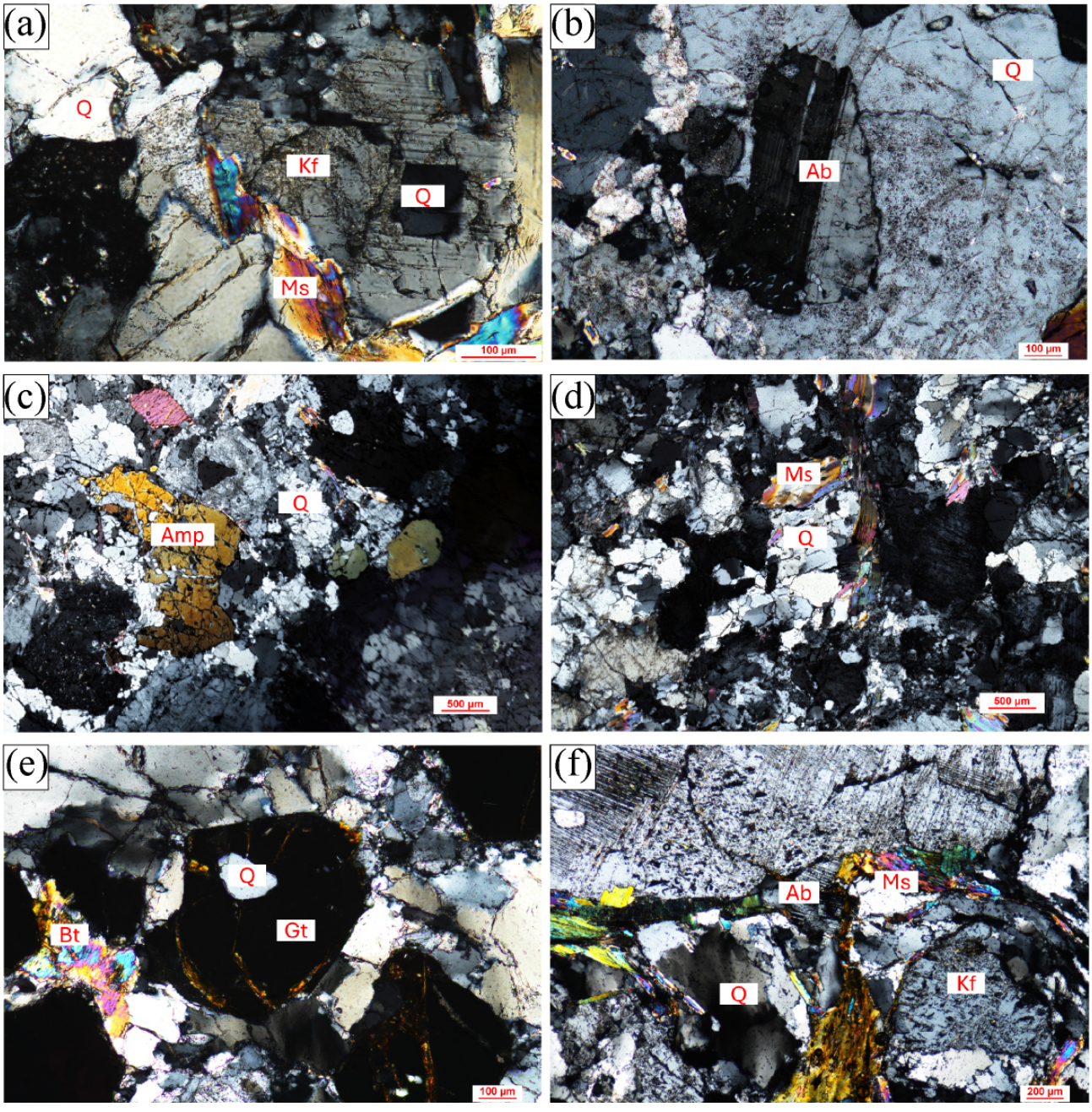

Figure 2. Representative photomicrographs of XZ-BG **(a, b, c)** and XZ-WJ **(d, e, f)**. Abbreviations: Q, quartz; Kf, K-feldspar; Ms, muscovite; Gt, garnet; Amp, amphibole; Bt, biotite.

Table 1. XRF analysis results of major elements (wt %) in leucogranites.

Major elements	Fe_2O_3	MnO	TiO_2	CaO	K_2O	SO_3	P_2O_5	SiO_2	Al_2O_3	Na_2O	MgO	Sum	ALK	A/NK	A / CNK
XZ-BG	0.55	0.017	0.041	0.25	5.28	0.001	0.13	74.68	14.78	3.37	0.099	99.20	8.65	1.313	1.262
XZ-WJ	0.11	0.019	0.014	0.28	3.7	0.001	0.059	73.73	15.16	5.15	0.055	98.28	8.85	1.215	1.167

Notes: ALK equates to $Na_2O + K_2O$ (%), A/NK equates to Al_2O_3 / ($Na_2O + K_2O$) (molecular number ratio), and A / CNK equates to Al_2O_3 / ($CaO + Na_2O + K_2O$) (molecular number ratio).

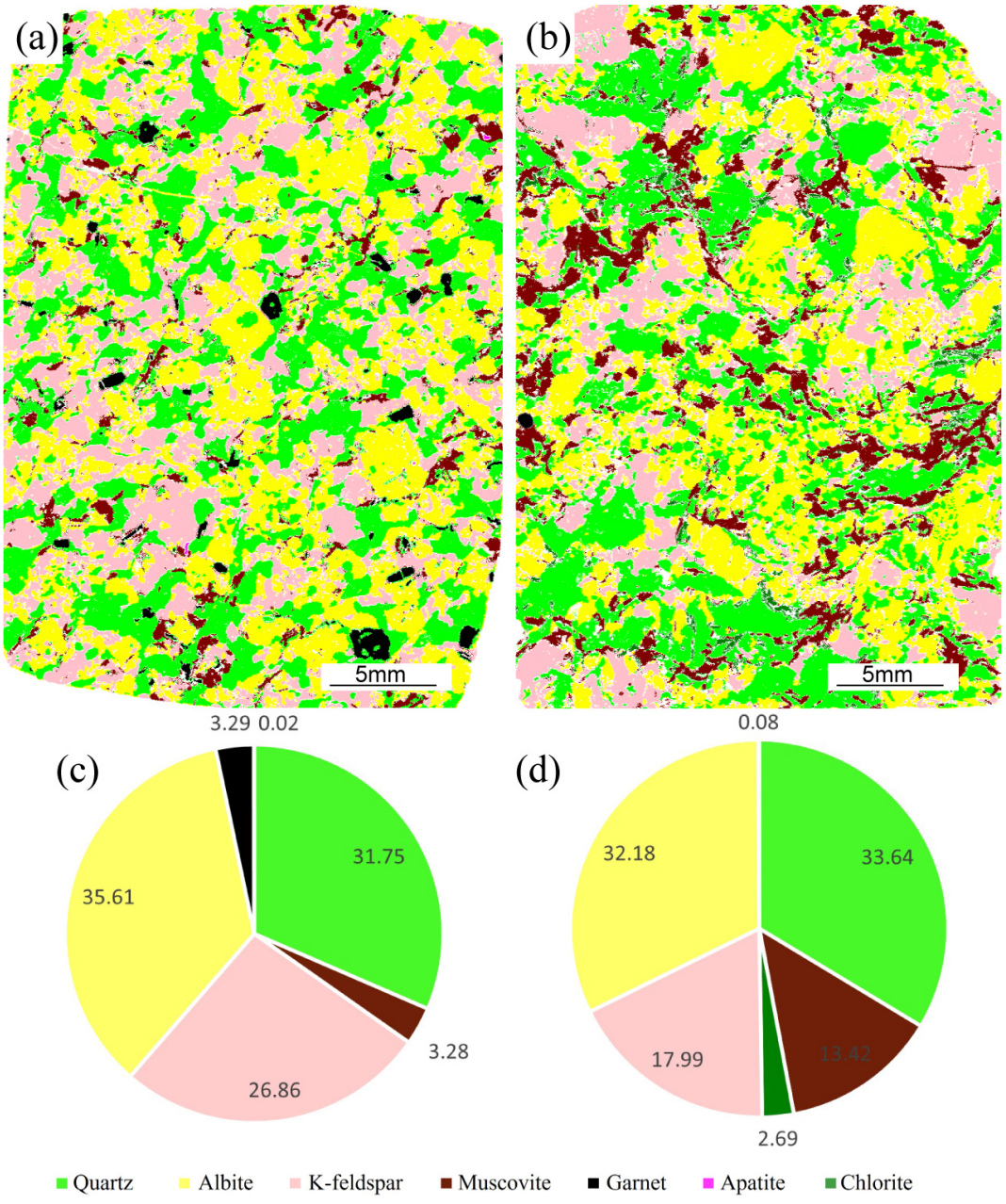

Figure 3. μ-XRF major element maps of the entirety of the thin sections and mineral mode pies for leucogranite XZ-BG **(a, c)** and leucogranite XZ-WJ **(b, d)**. The mineral types were determined through qualitative major element XRF spectra of the bulk thin sections. The pie chart data represent the ratio of the mass fraction of each mineral to the sum of the mass fractions of minerals in the thin section.

eraging 6.45 ppm, while Ge contents vary between 0.25 and 1.58 ppm, with a mean of 1.06 ppm. Additionally, K and Ca concentrations range from 0.65 to 20.28 ppm and from 10.26 to 128.10 ppm, respectively, with average values of 8.65 and 89.50 ppm. Quartz samples from XZ-WJ contain 5.12–13.58 ppm Li, 2.48–19.10 ppm Na, and 64.65–117.70 ppm Al, with average concentrations of 9.60, 7.78, and 89.95 ppm, respectively. Ti concentrations range from 2.52 to 5.16 ppm, averaging 3.87 ppm, while Ge contents vary between 0.48 and 1.91 ppm, with a mean of 1.19 ppm. K and Ca concentrations range from 5.31 to 19.63 and 10.90 to 152.60 ppm, respectively, with average values of 12.01 and 65.16 ppm.

Overall, compared with quartz from XZ-WJ, quartz from XZ-BG is characterized by lower Al, Li, and K concentrations but higher Ti and Na concentrations. Element–element plots (Fig. S3) illustrate the variability of trace element concentrations in quartz. In particular, Li, Na, and Ge display substantial scatter at a given Al concentration, and no well-

defined linear relationships are apparent for these element pairs.

4.4 Purification performance

4.4.1 Microscopic characteristics of inclusions and purification effects in quartz sand from samples

As shown in Fig. 4, the abundance, distribution patterns, and sizes of inclusions in the quartz sand of the two samples differ markedly before and after purification.

In sample XZ-BG, abundant inclusions are commonly observed in quartz grains before purification, and gas–liquid two-phase inclusions are dominant. Both primary and secondary inclusions occur: primary inclusions are typically arranged in planar arrays along quartz growth zones, whereas secondary inclusions commonly occur as linear trails associated with microfractures (Fig. 4a, b). The inclusions are mainly negative crystal-shaped and ellipsoidal, mostly ∼ 5–20 µm in size and most commonly ∼ 5–15 µm, whereas inclusions approaching 20 µm are rare. After purification, most quartz sand grains appear nearly inclusion-free and optically clean under optical microscopy (Fig. 4c). Their surfaces are rough and irregular, with distinct microcrack traces (Fig. 4d). Only a few grains still contain visible residual inclusions, which are mainly distributed in planar or irregular patterns and are extremely small, typically < 5 µm, whereas larger inclusions are almost absent.

In sample XZ-WJ, quartz grains also contain abundant inclusions before purification, likewise dominated by gas–liquid two-phase inclusions. The inclusions show diverse distribution patterns, including linear, planar, and irregular occurrences, and are generally finer-grained than those in XZ-BG; more than 70 % are < 10 µm in size (Fig. 4e, f). Two fluid inclusion assemblages can be distinguished: (1) inclusions aligned along quartz growth zones and (2) randomly dispersed clusters and isolated inclusions within quartz grains. After purification, most grains become nearly inclusion-free and optically clean under optical microscopy (Fig. 4g). The grain surfaces are rough and irregular and show distinct microcrack traces (Fig. 4h). Only a small number of extremely fine residual inclusions remain, mainly in planar or irregular distributions, and these are typically $<$ 5 µm in size.

4.4.2 Trace element characteristics of quartz before and after purification

To characterize the impurity levels of quartz prior to purification, the average values of in situ LA-ICP-MS spot analyses were used to represent the pre-purification trace element background (Table 2). Trace element contents of the purified quartz sand were determined by bulk digestion, with results summarized in Table 3, and the corresponding comparison is illustrated in Fig. 5.

For sample XZ-BG, the total impurity content decreased from 182.9 to 33.7 ppm after acid leaching and decreased further to 30.0 ppm following chlorination roasting. Specifically, Li decreased from 8.8 to 3.8 ppm after acid leaching and to 2.9 ppm after chlorination roasting; Na decreased from 19.4 to 2.8 ppm and then to 0.21 ppm; Mg decreased from 0.30 to 0.03 ppm after acid leaching; Al decreased from 60.2 to 19.1 ppm and decreased further to 18.8 ppm; K decreased from 6.8 to 0.31 ppm; Ca decreased from 74.7 to 0.68 ppm; Ti decreased from 7.0 to 6.2 ppm; and Fe decreased from 5.9 to 0.80 ppm and then to 0.48 ppm.

For sample XZ-WJ, total impurities decreased from 206.5 to 44.9 ppm after acid leaching and decreased further to 39.5 ppm following chlorination roasting. Li decreased from 9.8 to 7.8 ppm and then to 6.6 ppm; Na decreased from 8.0 to 3.3 ppm and then to 0.09 ppm; Mg decreased from 0.24 to 0.02 ppm; Al decreased from 89.5 to 28.6 ppm; K decreased from 11.1 to 0.68 ppm and decreased further to 0.61 ppm; Ca decreased from 69.9 to 0.18 ppm; Ti decreased from 4.0 to 3.9 ppm; and Fe decreased from 14.0 to 0.40 ppm and then to 0.35 ppm.

Overall, purification markedly reduced trace element contents in quartz from both XZ-BG and XZ-WJ, although the removal efficiencies varied significantly among different elements.

5 Discussion

5.1 Peraluminous S-type leucogranites: classification and source

Interpretation

Le Maitre (1976) classified granites based on their chemical variability; Streckeisen (1976) classified them according to the relative modal proportions of quartz, K-feldspar, and plagioclase, which have been shown to provide information about tectonic environments (Lameyre and Bowden, 1982). Shand (1927) and Tyrrell (1943) once classified granites based on their chemical composition into peraluminous, aluminous, and peralkaline types, leading to the widespread hypothesis that “calc-alkaline” granites are products of volcanic arc magmatism, “alkaline” and “peralkaline” magmas are related to intraplate environments, and “peraluminous” granites primarily form during continental collisions through deep melting of sedimentary rocks (Pearce et al., 1984). Chappell and White (1992, 2001) also classified granites into S-type and I-type based on geochemical characteristics, with S-type being considered to be a product of continental collisions and I-type originating from igneous or crustal sources (Regelous et al., 2021).

These classification schemes remain widely applied in granite studies. In this study, we employed these methods to classify leucogranite samples by plotting relevant geochemical data (Fig. S2), using background data from leucogranites

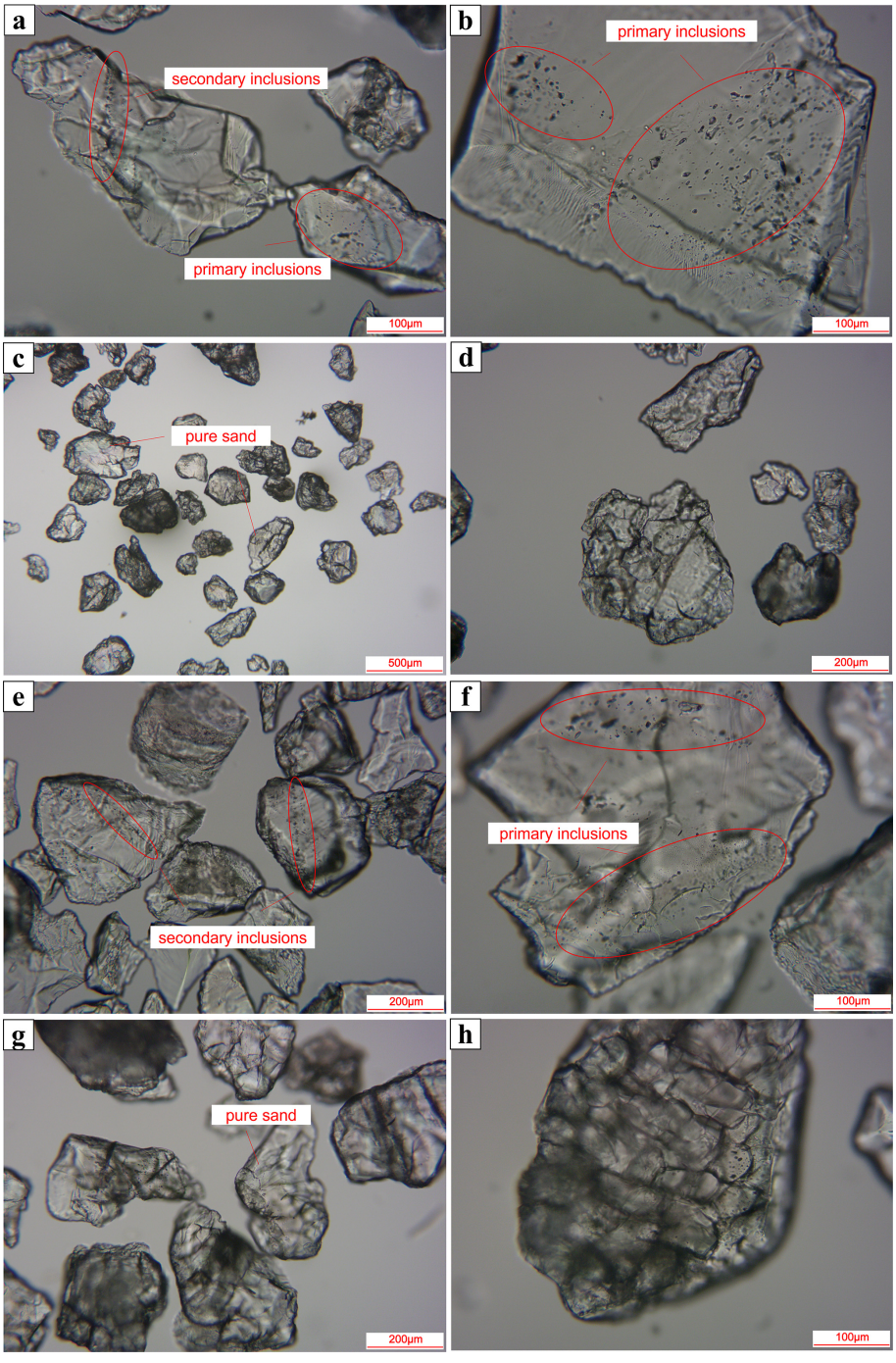

Figure 4. Inclusion characteristics of quartz sand. **(a, b)** Characteristics of inclusions in quartz sand from sample XZ-BG prior to purification. **(c, d)** Characteristics of inclusions in quartz sand from sample XZ-BG after purification. **(e, f)** Characteristics of inclusions in quartz sand from sample XZ-WJ prior to purification. **(g, h)** Characteristics of inclusions in quartz sand from sample XZ-WJ after purification.

of the Greater Himalaya Orogenic Belt. The samples showed strong consistency with these background datasets. On the TAS diagram, both samples fall within the granite field: XZ-WJ is a peraluminous high-potassium calc-alkaline granite, while XZ-BG is peraluminous, positioned between the alkali-calcic and high-potassium calc-alkaline series. Both samples are identified as S-type granites.

Strongly peraluminous S-type granites are generally considered to form through partial melting of upper crustal rocks that have experienced some degree of weathering (Clemens, 2003). Many studies relate Himalayan leucogranites to ana-

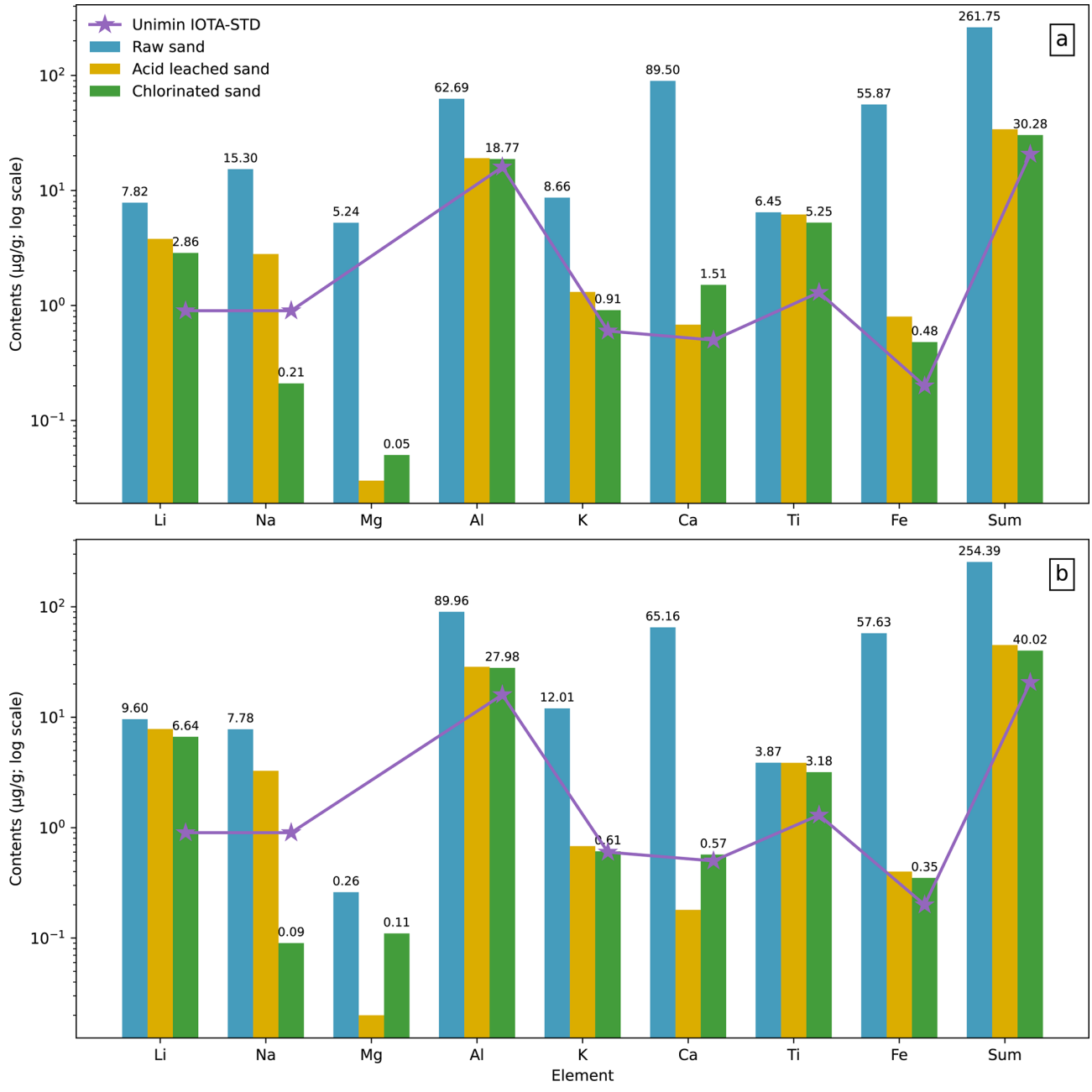

Figure 5. Comparison of impurity element contents in quartz from Tibetan leucogranites before and after purification and with Unimin IOTA-STD. **(a)** Sample XZ-BG. **(b)** Sample XZ-WJ.

texis within the Greater Himalaya Sequence (GHS) because leucogranite plutons are typically emplaced within high-grade Greater Himalayan sequence rocks and are spatially associated with migmatites; geochemical–isotopic constraints and melting experiments further support dehydration melting of GHS metapelites as a viable source (Le Fort et al., 1987; Searle and Godin, 2003; Inger and Harris, 1993; Patiño Douce and Harris, 1998). However, some authors have proposed that additional crustal components may also have contributed to leucogranite generation in order to explain isotopic heterogeneity within the Himalayan belt (Guo and Wilson, 2012; Hu et al., 2018).

In the present study, the Dinggye leucogranites are interpreted to have formed predominantly from a metasedimentary source, with a possible subordinate contribution from local granitic orthogneiss. This interpretation is supported by several lines of evidence. Notably, (1) some leucogranites in the Ama Drime-Dinggye area preserve inherited age components of ca. 1850–1800 Ma, consistent with the Paleoproterozoic protolith age of the local granitic orthogneiss.

Table 2. Results of in situ analysis of trace elements in quartz using laser ablation inductively coupled plasma mass spectrometry (LA-ICP-MS) and the temperature (°C) calculated from Ti.

	Li	B	Na	Mg	Al	P	K	Ca	Ti	Cr	Mn	Fe	Ni	Cu	Zn	Ge	T/°C
XZ-BG																	
01	6.90	1.89	3.63	3.93	63.46	26.66	10.76	120	5.56	1.45	0.76	493.8	2.1	0.12	9.18	0.92	530.59
02	6.56	0.37	5.97	45.27	64.77	48.17	11.34	11.85	5.69	8.37	0.49	7.35	3.5	0.28	3.43	0.25	536.17
03	3.30	0.44	7.86	1.14	77.26	98.54	17.11	240	4.64	1.63	0.87	16.58	36.99	0.75	4.10	1.41	526.89
04	10.95	2.79	12.72	0.17	67.57	26.18	20.28	106.4	9.16	2.00	0.34	4.44	0.96	1.00	0.72	1.02	569.55
05	12.7	1.12	28.93	0.09	72.59	42.92	0.65	63.4	7.06	1.13	0.54	5.16	0.90	0.09	0.59	1.37	548.81
06	8.32	1.21	18.84	1.34	70.15	51.89	1.75	38.57	7.04	2.60	0.71	11.18	0.95	0.78	0.76	1.44	548.57
07	6.83	1.55	36.91	0.04	49.50	85.28	14.25	128.1	6.35	3.88	1.15	9.80	1.37	1.30	1.08	0.93	540.59
08	10.03	3.25	3.06	0.04	60.51	40.03	3.19	10.26	7.20	0.55	0.45	0.25	0.83	0.40	0.53	1.33	550.33
09	8.10	0.51	31.48	0.16	60.15	33.06	2.03	105	6.41	1.60	0.58	9.87	1.71	1.01	0.71	0.33	541.37
10	4.56	0.98	3.57	0.24	40.92	45.17	5.24	71.37	5.40	1.68	0.37	0.26	1.16	0.80	0.47	1.58	528.42
Avg	7.82	1.41	15.30	5.24	62.69	49.79	8.65	89.50	6.45	2.49	0.63	55.87	5.05	0.65	2.16	1.06	548.13
XZ-WJ																	
01	10.2	1.98	11.57	0.61	103.8	22.62	16.81	53.53	3.40	0.30	0.04	5.68	1.09	0.67	1.73	1.22	495.34
02	8.99	4.10	4.46	0.58	97.26	58.09	19.63	10.9	2.52	4.74	0.22	457.4	1.36	0.30	119.2	0.83	506.95
03	5.81	4.57	19.1	0.23	99.89	55.76	16.66	129.8	2.92	0.33	0.78	43.26	1.24	1.43	5.38	0.48	451.42
04	8.91	7.68	3.33	0.35	117.7	49.26	12.34	84.33	3.62	2.13	1.24	26.52	1.12	0.56	1.71	0.65	514.17
05	5.12	4.84	2.48	0.28	72.5	15.03	10.85	152.6	4.10	2.32	1.30	1.05	2.46	0.78	1.04	1.91	508.53
06	13.44	3.35	5.29	0.13	85.55	36.42	5.31	27.88	5.16	1.22	0.27	7.35	1.47	1.51	1.87	1.60	525.07
07	12.59	0.50	10.23	0.21	81.11	9.55	7.43	19.25	4.03	1.27	0.03	2.40	1.19	0.48	10.45	1.52	507.35
08	9.00	2.84	5.60	0.01	64.65	22.04	9.78	70.45	4.71	1.87	0.46	14.09	1.09	0.24	0.78	0.97	518.45
09	13.58	4.07	6.29	0.10	90.69	34.78	9.27	21.12	3.97	1.35	0.22	11.91	0.96	1.16	1.43	1.33	506.28
10	8.34	3.55	9.42	0.12	86.46	16.59	12.03	81.77	4.24	2.92	0.48	6.68	0.75	0.35	0.94	1.38	510.87
Avg	9.60	3.75	7.78	0.26	89.95	32.01	12.01	65.16	3.87	1.85	0.51	57.63	1.27	0.75	14.45	1.19	504.44

Notes: 01, 02, 03, 04, 05, 06, 07, 08, 09, and 10 represents different positions.

Table 3. Trace element contents of purified quartz from leucogranites and Unimin standard sand.

Name	$W_B/10^{-6}$															W_B/%
	Al	B	Ca	Co	Cr	Cu	Fe	K	Li	Mg	Mn	Na	Ni	Ti	Sum	SiO_2
XZ-BG[a]	19.09	0.16	0.68	0.01	0.06	0.05	0.80	1.31	3.79	0.03	0.04	2.80	0.03	6.18	34.03	99.9966
XZ-BG[b]	18.77	0.17	1.51	0.01	0.01	0.01	0.48	0.91	2.86	0.05	0.03	0.21	0.01	5.25	30.28	99.9969
XZ-WJ[a]	28.63	0.28	0.18	0.01	0.06	0.06	0.40	0.68	7.82	0.02	0.05	3.27	0.04	3.86	45	99.9955
XZ-WJ[b]	27.98	0.31	0.57	0.01	0.09	0.01	0.35	0.61	6.64	0.11	0.03	0.09	0.04	3.18	40.02	99.9959
IOTA-STD	16.20	0.08	0.50	–	< 0.05	< 0.05	0.23	0.60	0.90	< 0.05	< 0.05	0.90	< 0.05	1.10	< 19.66	> 99.998

Note: [a] impurity elements and SiO_2 content of sample after acid leaching, [b] impurity elements and SiO_2 content of sample after chlorination roasting; IOTA-STD refers to the IOTA® high-purity-quartz sand produced by Unimin Corporation, used as a benchmark for comparison.

This suggests that orthogneissic material may have contributed to magma generation, although the presence of inherited ages alone does not provide definitive proof of source mixing (Cottle et al., 2009; Xu et al., 2005). (2) Yu et al. (2011) reported that Dinggye leucogranites are characterized by Rb enrichment and pronounced Sr depletion, resulting in high Rb/Sr. Rb is hosted predominantly in micas (muscovite/biotite), whereas Sr is mainly accommodated in plagioclase. Therefore, high Rb coupled with low Sr is consistent with partial melting of a mica-rich, plagioclase-poor metasedimentary upper crust, plausibly involving muscovite dehydration melting (Harris and Inger, 1992). (3) Dinggye leucogranites are typical peraluminous S-type granites, enriched in SiO_2, Al_2O_3, with high A / CNK, and contain abundant aluminum-rich minerals such as garnet, muscovite, and biotite, indicating a derivation from metamorphosed sedimentary rocks (Visonà and Lombardo, 2002; Gou et al., 2019).

5.2 Trace element characteristics of quartz grains

In the quartz lattice, Al is commonly incorporated through isomorphic substitution and generally exhibits the highest concentration among trace elements, providing significant environmental and petrogenetic information (Müller et al., 2012). Therefore, this study focuses on a graphical analysis of Al and its correlations with other trace elements in quartz (Fig. S3 in the Supplement).

During quartz crystallization, substitution of Si^{4+} by Al^{3+} requires charge compensation by coordinating ions (e.g., Li^+, Na^+, K^+, and H^+), which can lead to broadly coupled variations in these elements (Zhang et al., 2024b). In many quartz populations, Li^+ may be an important compensating ion for Al^{3+} (Jourdan et al., 2009); however, in the present samples, the Al–Li/Na/K relationships are dispersed, suggesting that charge compensation is variable and/or that minor non-lattice contributions may affect some analyses.

Trace element variations in quartz are influenced by lattice incorporation and inclusions. Although laser in situ measurements avoided visible inclusions, measured impurities may not exclusively represent lattice elements. Typically, substitutional ions (Al^{3+}, Fe^{3+}, B^{3+}) and interstitial ions (Li^+, Na^+, K^+, P^{5+}) occur in an approximately 1 : 1 ratio (Yang et al., 2022). In XZ-BG and XZ-WJ, the ratio $(Al^{3+} + Fe^{3+} + B^{3+}) / (Li^+ + Na^+ + K^+ + P^{5+})$ ranges from 0.72 to 1.14 and from 1.52 to 2.34, with average values of 0.95 and 1.88, respectively. The deviation from unity, especially in XZ-WJ, indicates that the measured trivalent-cation budget is not fully balanced by the measured monovalent budget in many spots, which may reflect variable charge compensation behavior and/or contributions from submicroscopic inclusions (Xie et al., 2022).

Al, Ge, and Ti in quartz have been linked to magmatic differentiation in previous studies, where Al and Ge tend to increase whereas Ti decreases with progressive differentiation (Schrön et al., 1988; Zhang et al., 2024a). In the Dinggye leucogranites, Al-Ti and Ge-Ti show only weak negative tendencies, and Al-Ge shows a weak positive tendency (Fig. S3), consistent with published datasets (Rusk et al., 2008). In this study, quartz from XZ-WJ has higher mean Al than that from XZ-BG; given the scatter in spot data, this difference is interpreted as reflecting variations in crystallization domains.

5.3 Ti contents in quartz as a constraint on crystallization temperatures of leucogranites

Müller et al. (2009) and Wark and Watson (2006) showed that Ti content in quartz serves as a critical geochemical indicator for recording magmatic crystallization temperatures, exhibiting a systematic correlation with the degree of magmatic evolution (fractionation extent). Specifically, as magmatic differentiation progresses, the Ti content incorporated in late-crystallized quartz displays a characteristic declining trend (Larsen et al., 2004; Götze et al., 2004). This phenomenon provides a robust theoretical foundation for reconstructing the crystallization temperatures of granitic magmatic systems using Ti-in-quartz content. In this study, we applied the Ti-in-quartz thermometry formula (Sect. S1.7 in the Supplement) proposed by Hayden and Watson (2007), which is specifically designed for rutile-absent systems, to accurately calculate the crystallization temperatures of two samples of leucogranite from the Dinggye area. Table 2 results show that the crystallization temperature of leucogranite XZ-BG ranges from 526 to 569 °C, with an average temperature of approximately 542 °C; the crystallization temperature of leucogranite XZ-WJ ranges from 451 to 525 °C, with an average temperature of approximately 504 °C. The crystallization temperature of XZ-BG is higher than that of XZ-WJ. Based on previous theories, this temperature difference may suggest that XZ-WJ represents a relatively more evolved melt fraction formed during late-stage differentiation within the same magmatic system. Magma with a higher degree of differentiation generally has a longer evolution time and crystallizes later, and its final crystallization temperature is also lower. The crystallization temperatures of these two sets of leucogranite (451–569 °C) calculated in this study are significantly lower than the commonly accepted solidus temperature range for granite systems, which is generally considered to be between 650 and 700 °C (Steiner et al., 1975). It strongly proves that the leucogranite magma in the Himalayan crystallization region has the potential to evolve to temperatures below the solidus temperature of traditional granite magma systems. This means that magmas in this region can sustain its residual melt (or fluid) and ultimately crystallize into leucogranite at very low temperatures (below 650 °C), even below the solidus temperature for typical granite magmas. This low-temperature crystallization phenomenon may be closely related to the geological conditions of igneous crystallization in the Himalayan region. The source area is rich in water and volatiles (such as F and B), and these components are effective fluxes that can significantly lower the solidus temperature of magma (Tuttle and Bowen, 1958; Holtz et al., 1995; London, 1987; Gao et al., 2017). A shallow emplacement under low-pressure conditions can favor the stabilization of hydrous, low-melting-point minerals and thus promote crystallization at relatively low temperatures (Luth et al., 1964; Scaillet et al., 1995). In addition, slow cooling of the shallowly emplaced leucogranitic magma allows a volatile-rich residual melt to be maintained over a prolonged temperature interval. This extended residence time at low temperatures facilitates continued differentiation and promotes more complete crystallization of late-stage melts (Huang and Audétat, 2012). Therefore, the observed unusually low crystallization temperatures provide important constraints on melt evolution and emplacement processes in collisional orogenic belts, helping to clarify how leucogranitic magmas differentiate and solidify during crustal thickening and exhumation.

5.4 Significance of high-purity-quartz raw ore from leucogranites

The occurrence and concentration of impurities in high-purity-quartz (HPQ) raw ore are key factors determining the quality of the final product. Impurities are generally classified into three types: symbiotic gangue minerals, inclusions, and lattice impurities (Yang et al., 2022). Symbiotic

gangue minerals coexist with quartz during mineralization, varying according to geological conditions. Common associated minerals include feldspar, mica, rutile, hematite, magnetite, tourmaline, fluorite, epidote, and calcite (Courba et al., 2025). Inclusions, captured during quartz crystallization, can be solid, liquid, or gaseous. They are classified as primary (formed during crystal growth on faces, most difficult to remove), pseudosecondary (formed during stress-induced cracks and subsequently trapped), and secondary (formed post-crystallization in intergranular cracks, easier to remove) (Shi et al., 2023). Inclusions can also be classified as mineral, melt, or fluid inclusions, with fluid inclusions – comprising H_2O, CO_2, CH_4, N_2, and hydrocarbons – being most abundant. Inclusions affect purification by introducing impurities and producing etch pits that generate bubbles in quartz glass. Quartz lattice impurities are formed when other metal or non-metal ions substitute silicon atoms in the quartz lattice, and they are closely related to the point defects in the quartz crystal (Stalder, 2021). The point defects in quartz crystals include vacancies, substitutional atoms, and interstitial atoms, with the latter two being the primary modes of lattice impurity element introduction. Foreign impurity ions such as Ti^{4+}, Ge^{4+}, Al^{3+}, B^{3+}, Fe^{3+}, and P^{5+} substitute for Si^{4+}, forming substitutional impurity elements. At the same time, when certain non-tetravalent ions replace Si^{4+}, compensation ions like K^+, Na^+, and Li^+ are introduced into the atomic gaps to maintain electrical charge balance, forming interstitial impurity elements (Larsen et al., 2004). These lattice impurities are difficult to remove from quartz using existing purification processes.

Considering the fact that leucogranite forms in high-temperature environments and the incorporation mechanisms of impurity elements in quartz, elements such as Ti and Al can easily enter the quartz lattice structure in large quantities. This makes leucogranite difficult to use as a raw material for purifying high-purity quartz. However, Himalayan leucogranite has a relatively low crystallization temperature, typically below 800 °C (Cisneros et al., 2020). Studies show that the zircon saturation temperature range for most Himalayan leucogranite is between 650 and 750 °C (Xie, 2023; Gao et al., 2024; Aikman et al., 2012). In this study, using the quartz-Ti thermometer, the formation temperature of leucogranite samples was calculated to be between 451 and 569 °C, indicating that the formation conditions are similar to those of pegmatitic crystallization temperatures and pressures, providing a source of high-purity-quartz raw material.

Table 3 shows that quartz grains from the XZ-BG and XZ-WJ leucogranite samples after the final purification process contain 99.9969 wt % and 99.9959 wt % SiO_2, respectively (Table 3). Al and Ti contents are typically used as indicators of quartz quality because these elements are among the most common and hardest-to-remove trace elements. Quartz grain samples were plotted in the Al–Ti high-purity-quartz classification diagram (Müller et al., 2007), and both samples fall within the high-purity-quartz field (Fig. 6). However, compared with the benchmark high-purity-quartz sand produced by Unimin (IOTA® standard), regarded as a benchmark material in HPQ research and industry because of its exceptionally high purity and extremely low trace element contents, the residual Li and Ti contents of purified quartz grains are still relatively high (Fig. 5). This indicates that, although the quartz grains from Dinggye leucogranites could meet the HPQ field in terms of Al–Ti contents, a further reduction in Li and other trace elements such as Ti would be required to approach the IOTA® benchmark level.

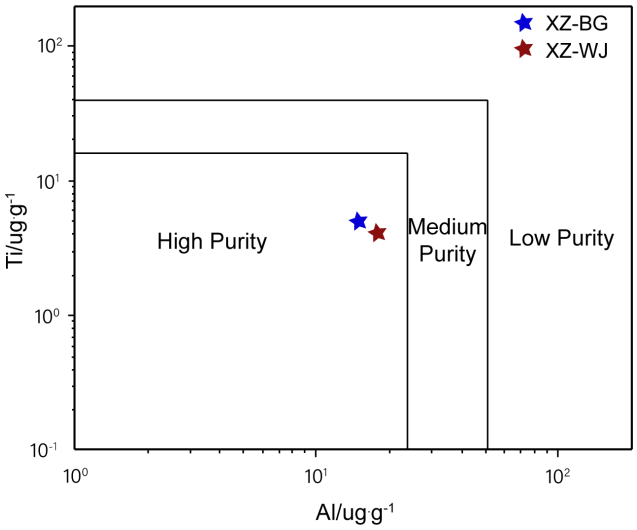

Figure 6. Al vs. Ti plot of quartz in leucogranites from Tibet (after Müller et al., 2007).

6 Conclusion

The XZ-BG and XZ-WJ samples from the Dinggye leucogranite body in Tibet are both classified as peraluminous S-type leucogranites, likely derived from a source region composed of gneissic and metamorphosed shale materials. The charge compensation mechanisms and coordination modes of impurities in the quartz lattice are relatively complex, and, overall, the samples crystallized in a low-temperature mineralization environment comparable to that of pegmatites. Ti-in-quartz thermometry indicates average quartz crystallization temperatures of approximately 542 °C for XZ-BG and 504 °C for XZ-WJ. Purification experiments demonstrate that inclusion-related impurities in quartz can be effectively removed, yielding final products with SiO_2 contents of 99.9969 wt % and 99.9959 wt %, respectively. Although residual Li and Ti concentrations remain relatively higher than those of IOTA®, both samples plot within the high-purity-quartz field on the Al–Ti discrimination diagram, suggesting that even higher-purity quartz could be achieved through further optimization of the purification process. Overall, this study confirms that Dinggye

leucogranite can serve as a promising source of quartz with favorable purification potential. It also highlights that exploration and raw-material evaluation should consider not only the distribution of leucogranite bodies but also the trace element composition of quartz, crystallization temperatures, and residual impurity characteristics after purification. These findings provide a solid foundation for the further investigation and assessment of leucogranite-hosted high-purity-quartz resources in Tibet.

Data availability. All data derived from this research are presented in Figs. 1–6, S1–S3 and in Tables 1–3.

Supplement. The supplement related to this article is available online at https://doi.org/10.5194/ejm-38-249-2026-supplement.

Author contributions. LS: responsible for designing the experimental protocol, performed the majority of the experiments and data collection, conducted data analysis, and drafted the initial paper. XY: responsible for conceptualization and funding acquisition; supervised the entire research project; and reviewed, edited, and finalized the paper. MX: critically reviewed and revised the paper for important intellectual content. YQ: helped in the flotation experiment ZH: assistance in the sample data-testing process. XF, ZC: provided assistance during the sample collection process.

Competing interests. The contact author has declared that none of the authors has any competing interests.

Disclaimer. Publisher's note: Copernicus Publications remains neutral with regard to jurisdictional claims made in the text, published maps, institutional affiliations, or any other geographical representation in this paper. The authors bear the ultimate responsibility for providing appropriate place names. Views expressed in the text are those of the authors and do not necessarily reflect the views of the publisher.

Acknowledgements. We greatly appreciate the assistance of the students in the Quartz Laboratory with the purification experiments.

Financial support. This study was financially supported by grants from the National Key Research and Development Program on Strategic Mineral Resources Development and Utilization (grant no. 2024YFC2910101) and projects from the China Geological Survey (grant nos. DD20211555 and DD20220989).

Review statement. This paper was edited by Rubén Piña and reviewed by two anonymous referees.

References

Aikman, A. B., Harrison, T. M., and Hermann, J.: Age and thermal history of Eo- and Neohimalayan granitoids, eastern Himalaya, J. Asian Earth Sci., 51, 85–97, https://doi.org/10.1016/j.jseaes.2012.01.011, 2012.

Cao, H., Pei, Q., Santosh, M., Li, G., Zhang, L., Zhang, X., Zhang, Y., Zou, H., Dai, Z., Lin, B., Tang, L., and Yu, X.: Himalayan leucogranites: A review of geochemical and isotopic characteristics, timing of formation, genesis, and rare metal mineralization, Earth-Sci. Rev., 234, 104229, https://doi.org/10.1016/j.earscirev.2022.104229, 2022.

Chappell, B. W. and White, A. J. R.: I- and S-type granites in the Lachlan Fold Belt, in: The Second Hutton Symposium on the Origin of Granites and Related Rocks, Geol. Soc. Am. Spec. Pap., 272, 1–26, https://doi.org/10.1130/SPE272-p1, 1992.

Chappell, B. W. and White, A. J. R.: Two contrasting granite types: 25 years later, Aust. J. Earth Sci., 48, 489–499, https://doi.org/10.1046/j.1440-0952.2001.00882.x, 2001.

Cisneros, M., Ashley, K. T., and Bodnar, R. J.: Evaluation and application of the quartz-inclusions-in-epidote mineral barometer, Am. Mineral., 105, 1140–1151, https://doi.org/10.2138/am-2020-7379, 2020.

Clemens, J. D.: S-type granitic magmas-petrogenetic issues, models and evidence, Earth-Sci. Rev., 61, 1–18, https://doi.org/10.1016/S0012-8252(02)00107-1, 2003.

Courba, S., Hahou, Y., Achmani, J., El Basbas, A., Ouallali, A., Aafir, Z., Sassioui, S., Ousaid, L., and El Amrani, M.: Paragenesis and supergene evolution of the Cu-Ba ± Pb-Amethyst mineralization from Baba Joua Ali, Eastern Anti-Atlas, Morocco: Exploration application, J. Afr. Earth Sci., 223, 105466, https://doi.org/10.1016/j.jafrearsci.2024.105466, 2025.

Cottle, J. M., Jessup, M. J., Newell, D. L., Horstwood, M. S. A., Noble, S. R., Parrish, R. R., Waters, D. J., and Searle, M. P.: Geochronology of granulitized eclogite from the Ama Drime Massif: Implications for the tectonic evolution of the South Tibetan Himalaya, Tectonics, 28, TC1004, https://doi.org/10.1029/2008TC002256, 2009.

DiPietro, J. A. and Pogue, K. R.: Tectonostratigraphic subdivisions of the Himalaya: A view from the west, Tectonics, 23, TC5001, https://doi.org/10.1029/2003TC001554, 2004.

Gao, L.-E., Zeng, L., and Asimow, P. D.: Contrasting geochemical signatures of fluid-absent versus fluid-fluxed melting of muscovite in metasedimentary sources: The Himalayan leucogranites, Geology, 45, 39–42, https://doi.org/10.1130/G38336.1, 2017.

Gao, P., Huang, H., Yin, C., Zhang, J., and Qian, J.: Himalayan leucogranites are hotter than previously thought, Chin. Sci. Bull., 69, 2682–2694, https://doi.org/10.1360/TB-2023-0827, 2024 (in Chinese).

Götze, J., Plötze, M., Graupner, T., Hallbauer, D. K., and Bray, C. J.: Trace element incorporation into quartz: A combined study by ICP-MS, electron spin resonance, cathodoluminescence, capillary ion analysis, and gas chromatography, Geochim. Cosmochim. Ac., 68, 3741–3759, https://doi.org/10.1016/j.gca.2004.01.003, 2004.

Gou, Z., Dong, X., and Wang, B.: Petrogenesis and Tectonic Implications of the Paiku Leucogranites, Northern Himalaya, J. Earth

Sci., 30, 525–534, https://doi.org/10.1007/s12583-019-1219-8, 2019.

Gu, D., Zhang, J., Lin, C., Fan, Y., Feng, L., Zheng, J., and Liu, S.: Anatexis and resultant magmatism of the Ama Drime Massif: Implications for Himalayan mid-Miocene tectonic regime transition, Lithos, 424–425, 106773, https://doi.org/10.1016/j.lithos.2022.106773, 2022.

Guo, Z. F. and Wilson, M.: The Himalayan leucogranites: Constraints on the nature of their crustal source region and geodynamic setting, Gondwana Res., 22, 360–376, https://doi.org/10.1016/j.gr.2011.07.027, 2012.

Hao, W., Feng, S., Zhan, J., Zhang, X., and Li, G.: Global high-purity quartz resource status, production, consumption and trade patterns, China Non-metallic Minerals Industry, 05 , 15–19, 2020 (in Chinese).

Harben, P. W.: The industrial minerals handy book: A guide to markets, specifications, & prices, 2nd edn., Industrial Minerals Division, Metal Bulletin, UK, 296 pp., http://pascal-francis.inist.fr/vibad/index.php?action=getRecordDetail&idt=6190195 (last access: 15 December 2025), 1995.

Harris, N. B. W. and Inger, S.: Trace element modelling of pelite-derived granites, Contrib. Mineral. Petrol., 110, 46–56, https://doi.org/10.1007/BF00310881, 1992.

Hayden, L. A. and Watson, E. B.: Rutile saturation in hydrous siliceous melts and its bearing on Ti-thermometry of quartz and zircon, Earth Planet. Sci. Lett., 258, 561–568, https://doi.org/10.1016/j.epsl.2007.04.020, 2007.

Holtz, F., Behrens, H., Dingwell, D. B., and Johannes, W.: H_2O solubility in haplogranitic melts: Compositional, pressure, and temperature dependence, Am. Mineral., 80, 94–108, https://doi.org/10.2138/am-1995-1-210, 1995.

Hou, Z., Zhang, H., Pan, X., and Yang, Z.: Porphyry Cu (-Mo-Au) deposits related to melting of thickened mafic lower crust: Examples from the eastern Tethyan metallogenic domain, Ore Geol. Rev., 39, 21–45, https://doi.org/10.1016/j.oregeorev.2010.09.002, 2011.

Hu, G., Zeng, L., Gao, L.-E., Liu, Q., Chen, H., and Guo, Y.: Diverse magma sources for the Himalayan leucogranites: Evidence from B-Sr-Nd isotopes, Lithos, 314–315, 88–99, https://doi.org/10.1016/j.lithos.2018.05.022, 2018.

Huang, R. and Audétat, A.: The titanium-in-quartz thermometer: A critical examination and re-calibration, Geochim. Cosmochim. Ac., 84, 75–89, https://doi.org/10.1016/j.gca.2012.01.009, 2012.

Inger, S. and Harris, N.: Geochemical constraints on leucogranite magmatism in the Langtang Valley, Nepal Himalaya, J. Petrol., 34, 345–368, https://doi.org/10.1093/petrology/34.2.345, 1993.

Jourdan, A.-L., Vennemann, T. W., Mullis, J., Ramseyer, K., and Spiers, C. J.: Evidence of growth and sector zoning in hydrothermal quartz from Alpine veins, Eur. J. Mineral., 21, 219–231, https://doi.org/10.1127/0935-1221/2009/0021-1881, 2009.

Lameyre, J. and Bowden, P.: Plutonic rock types series: Discrimination of various granitoid series and related rocks, J. Volcanol. Geoth. Res., 14, 169–186, https://doi.org/10.1016/0377-0273(82)90047-6, 1982.

Langille, J. M., Jessup, M. J., Cottle, J. M., Newell, D. L., and Seward, G.: Kinematic evolution of the Ama Drime detachment: Insights into orogen-parallel extension and exhumation of the Ama Drime Massif, Tibet-Nepal, J. Struct. Geol., 32, 900–919, https://doi.org/10.1016/j.jsg.2010.04.005, 2010.

Larsen, R. B., Henderson, I., Ihlen, P. M., and Jacamon, F.: Distribution and petrogenetic behaviour of trace elements in granitic pegmatite quartz from South Norway, Contrib. Mineral. Petrol., 147, 615–628, https://doi.org/10.1007/s00410-004-0580-4, 2004.

Le Fort, P., Cuney, M., Deniel, C., France-Lanord, C., Sheppard, S. M. F., Upreti, B. N., and Vidal, P.: Crustal generation of the Himalayan leucogranites, Tectonophysics, 134, 39–57, https://doi.org/10.1016/0040-1951(87)90248-4, 1987.

Le Maitre, R. W.: The Chemical Variability of Some Common Igneous Rocks, J. Petrol., 17, 589–598, https://doi.org/10.1093/petrology/17.4.589, 1976.

London, D.: Internal differentiation of rare-element pegmatites: Effects of boron, phosphorus, and fluorine, Geochim. Cosmochim. Ac., 51, 403–420, https://doi.org/10.1016/0016-7037(87)90058-5, 1987.

Luth, W. C., Jahns, R. H., and Tuttle, O. F.: The granite system at pressures of 4 to 10 kilobars, J. Geophys. Res., 69, 759–773, https://doi.org/10.1029/JZ069i004p00759, 1964.

Magar, J. T., Yang, X., Li, K., Xia, M., Li, X., and Cai, Z.: Mineralogical characteristics and purification experiments of quartz from a pegmatite: a case study in the Lushi region of the Qinling orogenic belt, central China, Minerals, 14, 1225, https://doi.org/10.3390/min14121225, 2024.

Müller, A., Ihlen, P. M., Wanvik, J. E., and Flem, B.: High-purity quartz mineralisation in kyanite quartzites, Norway, Miner. Deposita, 42, 523–535, https://doi.org/10.1007/s00126-007-0124-8, 2007.

Müller, A., van den Kerkhof, A. M., Behr, H.-J., Kronz, A., and Koch-Müller, M.: The evolution of late-Hercynian granites and rhyolites documented by quartz – a review, Earth Environ. Sci. Trans. R. Soc. Edinb., 100, 185–204, https://doi.org/10.1017/S1755691009016144, 2009.

Müller, A., Wanvik, J. E., and Ihlen, P. M.: Petrological and chemical characterisation of high-purity quartz deposits with examples from Norway. Quartz: Deposits, Mineralogy and Analytics, Springer Berlin Heidelberg, Germany, 71–118, https://doi.org/10.1007/978-3-642-22161-3_4, 2012.

Najman, Y., Appel, E., Boudagher-Fadel, M., Bown, P., Carter, A., Garzanti, E., Godin, L., Han, J., Liebke, U., Oliver, G., Parrish, R., and Vezzoli, G.: Timing of India-Asia collision: Geological, biostratigraphic, and palaeomagnetic constraints, J. Geophys. Res.-Sol. Ea., 115, B12416, https://doi.org/10.1029/2010JB007673, 2010.

Patiño Douce, A. E. and Harris, N.: Experimental constraints on Himalayan anatexis, J. Petrol., 39, 689–710, https://doi.org/10.1093/petrology/39.4.689, 1998.

Pearce, J. A., Harris, N. B. W., and Tindle, A. G.: Trace element discrimination diagrams for the tectonic interpretation of granitic rocks, J. Petrol., 25, 956–983, https://doi.org/10.1093/petrology/25.4.956, 1984.

Regelous, A., Scharfenberg, L., and De Wall, H.: Origin of S-, A- and I-Type Granites: Petrogenetic Evidence from Whole Rock Th/U Ratio Variations, Minerals, 11, 672, https://doi.org/10.3390/min11070672, 2021.

Rusk, B. G., Lowers, H. A., and Reed, M. H.: Trace elements in hydrothermal quartz: Relationships to cathodoluminescent textures and insights into vein formation, Geology, 36, 547–550, https://doi.org/10.1130/G24580A.1, 2008.

Searle, M. P. and Godin, L.: The South Tibetan Detachment and the Manaslu leucogranite: a structural reinterpretation and restoration of the Annapurna-Manaslu Himalaya, Nepal, J. Geol., 111, 505–523, https://doi.org/10.1086/376763, 2003.

Scaillet, B., Pichavant, M., Eymard, A., Bourdier, J. L., and Roux, J.: Experimental crystallization of leucogranite magmas, J. Petrol., 36, 663–705, https://doi.org/10.1093/petrology/36.3.663, 1995.

Schrön, W., Schmädicke, E., Thomas, R., and Smith, W.: Geochemische Untersuchungen an Pegmatitquarzen, Z. Geol. Wiss., 16, 229–244, 1988.

Shand, S. J.: On the Relations between Silica, Alumina, and the Bases in Eruptive Rocks, Considered as a Means of Classification, Geol. Mag., 64, 446–449, https://doi.org/10.1017/S0016756800103760, 1927.

Shi, Y., Wang, X., Zhang, H., Yan, H., and Liang, Q.: Research progress on impurity types and deep purification technology of high-purity quartz, Papermaking Equipment and Materials, 52, 76–78, 2023 (in Chinese).

Stalder, R.: OH point defects in quartz – a review, Eur. J. Mineral., 33, 145–163, https://doi.org/10.5194/ejm-33-145-2021, 2021.

Steiner, J. C., Jahns, R. H., and Luth, W. C.: Crystallization of alkali feldspar and quartz in the haplogranite system $NaAlSi_3O_8$-$KAlSi_3O_8$-SiO_2-H_2O at 4 Kb, Geol. Soc. Am. Bull., 86, 83–98, https://doi.org/10.1130/0016-7606(1975)86<83:COAFAQ>2.0.CO;2, 1975.

Streckeisen, A.: To Each Plutonic Rock Its Proper Name, Earth-Sci. Rev., 12, 1–33, https://doi.org/10.1016/0012-8252(76)90052-0, 1976.

Tuttle, O. F. and Bowen, N. L.: Origin of granite in the light of experimental studies in the system NaAlSi3O8-KAlSi3O8-SiO_2-H_2O, Mem. Geol. Soc. Am., 74, 153, https://doi.org/10.1130/MEM74, 1958.

Tyrrell, G. W.: Eruptive Rocks, Nature, 152, 433, https://doi.org/10.1038/152433a0, 1943.

Visonà, D. and Lombardo, B.: Two-mica and tourmaline leucogranites from the Everest-Makalu region (Nepal-Tibet). Himalayan leucogranite genesis by isobaric heating?, Lithos, 62, 125–150, https://doi.org/10.1016/S0024-4937(02)00112-3, 2002.

Wang, R. C., Wu, F. Y., Xie, L., Liu, X. C., Wang, J. M., Yang, L., Lai, W., and Liu, C.: A preliminary study of rare-metal mineralization in the Himalayan leucogranite belts, South Tibet, Sci. China Earth Sci., 60, 1655–1663, https://doi.org/10.1007/s11430-017-9075-8, 2017b.

Wang, Y. H., Zhang, L. F., Li, S. Z., and Somerville, I.: Zircon U-Pb dating and phase equilibria modelling of gneisses from Dinggye area, Ama Drime Massif, central Himalaya, Geol. J., 52, 476–494, https://doi.org/10.1002/gj.3027, 2017a.

Wark, D. A. and Watson, E. B.: TitaniQ: a titanium-in-quartz geothermometer, Contrib. Mineral. Petrol., 152, 743–754, https://doi.org/10.1007/s00410-006-0132-1, 2006.

Wu, F. Y., Liu, Z. C., Liu, X. C., and Ji, W. Q.: Himalayan leucogranite: Petrogenesis and implications to orogenesis and plateau uplift, Acta Petrol. Sin., 31, 1–36, 2015 (in Chinese).

Xie, Z. F.: Analysis of impurity characteristics and genesis of quartz ore in Fujia Mountain, southeastern Hubei, Master's thesis, Yangtze University, 2023.

Xie, Z. F., Wang, J. Y., Peng, Y. C., and Hu, Y. F.: Impurity characteristics of quartz ore from the Fujiashan Range in southeastern Hubei and its potential as a raw material for high-purity quartz, Acta Petrol. Mineral., 41, 1159–1168, 2022 (in Chinese).

Xu, Z. Q., Yang, J. S., Liang, F. H., Qi, X. X., Liu, F. L., Zeng, L. S., Liu, D. Y., Li, H. B., Wu, C. L., Shi, R. D., and Chen, S. Y.: Pan-African and Early Paleozoic Orogenic Events in the Himalaya Terrane: Inference from SHRIMP U-Pb Zircon Ages, Acta Petrol. Sin., 21, 1–12, 2005 (in Chinese).

Yang, X., Sun, C., Cao, J., and Shi, J.: High purity quartz: Research progress and perspective review, Earth Sci. Front., 29, 231–244, https://doi.org/10.13745/j.esf.sf.2021.8.1, 2022.

Yin, A.: Cenozoic tectonic evolution of the Himalayan orogen as constrained by along-strike variation of structural geometry, exhumation history, and foreland sedimentation, Earth-Sci. Rev., 76, 1–131, https://doi.org/10.1016/j.earscirev.2005.05.004, 2006.

Yu, J., Zeng, L. S., Liu, J., Gao, L., and Xie, K.: The formation mechanism and tectonic dynamic significance of the Early Miocene leucogranite in Dinggye area, southern Tibet, China, Acta Petrol. Sin., 27, 1961–1972, 2011 (in Chinese).

Zhang, H., Zou, S., Chen, X., Xu, D., Wang, Z., Zhang, Y., and Wang, H.: Unveiling Nb-Ta mineralization processes: Insight from quartz textural and chemical characteristics in the Songshugang deposit, Jiangxi Province, South China, Acta Geochim., 43, 737–753, https://doi.org/10.1007/s11631-024-00705-2, 2024a.

Zhang, J., Santosh, M., Wang, X., Guo, L., Yang, X., and Zhang, B.: Tectonics of the northern Himalaya since the India-Asia collision, Gondwana Res., 21, 939–960, https://doi.org/10.1016/j.gr.2011.11.004, 2012.

Zhang, L., Liu, L., Zhu, L., Wang, H., and Yuan, Y.: Discussion on the geological evaluation for high purity quartz raw material, Acta Petrol. Sin., 40, 1311–1326, https://doi.org/10.18654/1000-0569/2024.04.16, 2024b (in Chinese).

Zhou, H., Müller, A., and Berndt, J.: Quartz chemistry fingerprints melt evolution and metamorphic modifications in high-purity quartz deposits, Geochim. Cosmochim. Ac., 356, 179–195, https://doi.org/10.1016/j.gca.2023.07.015, 2023.

Zhou, Q. F., Qin, K. Z., He, C. T., Wu, H. Y., Liu, Y. C., Niu, X. L., Mo, L. C., Liu, X. C., and Zhao, J. X.: Li-Be-Nb-Ta mineralogy of the Kuqu leucogranite and pegmatite in the Eastern Himalaya, Tibet, and its implication, Acta Petrol. Sin., 37, 3305–3324, https://doi.org/10.18654/1000-0569/2021.11.05, 2021 (in Chinese).